# Influence of hydrogen content and injection scheme on the describing function of swirled flames

Thierry Schuller, Sylvain Marragou, Gorkem Oztarlik, Thierry Poinsot, Laurent Selle

# Influence of hydrogen content and injection scheme on the describing function of swirled flames

T. Schuller[a,*], S. Marragou[a], G. Oztarlik[a], T. Poinsot[a], L. Selle[a]

[a] *Institut de Mécanique des Fluides de Toulouse, IMFT, Université de Toulouse, CNRS, Toulouse, France*

**Abstract**

The dynamics of V-shape swirled lean premixed methane/air flames enriched with hydrogen is examined for two injection schemes. The response of the flames submitted to harmonic flowrate modulations is compared when hydrogen is premixed with the main methane/air flow and when it is injected pure as a pilot jet, directly at the flame base. Experiments are carried out at constant thermal power. Results obtained for the flame describing function (FDF) show that for a given hydrogen content, the premixed and pilot injection strategies lead to drastically different responses, although the shape of these flames are close. In the fully premixed strategy, the frequency bandwidth over which the flame is very responsive widens as the flame shortens due to the higher reactivity of the hydrogen enriched combustible mixture. Increasing the hydrogen content leads to an increased receptivity of the premixed flame sheet to incident flow perturbations. The opposite effect is seen for the pilot injection strategy due to a rebalancing of the heat release rate distribution along the flame brush with higher reaction rates close to the flame base compared to the reference methane/air case and the fully premixed hydrogen injection strategies. With hydrogen pilot injection, heat release rate fluctuations at the flame base interfere with those further downstream along the reaction layer, leading to an overall reduction of the FDF gain. This mechanism is evidenced with a set of experiments and confirmed by a low order model that considers a non uniform distribution of the heat release along a wrinkled flame sheet. It is also shown to persist when the forcing level is varied. These experiments indicate that the FDF of swirling V-flames can be lowered over a broad frequency range with hydrogen piloting due to a higher reactivity at the flame base.

*Keywords:*
Swirled flames, Hydrogen, Flame Transfer Function, Pilot injection

## 1. Introduction

Determining the response of flames submitted to imposed flow perturbations is a powerful way to analyze the susceptibility of combustors to thermo-acoustic instabilities [1–6]. In the frequency space, this response corresponds to the Flame Transfer Function (FTF) in the linear regime [7, 8] or Flame Describing Function (FDF) when perturbations of finite amplitudes are considered [9, 10]. Tailoring the gain and phase lag of the FTF/FDF to some desired shape appears in turn as a natural way to augment the stability margins of a combustor [11].

There are different ways to alter the FTF/FDF. One may act on the distribution of air and fuel mass flowrates in the burner to modify the fuel stratification [12]. Another possibility is to change the structure of the flow by tweaking the aerodynamics through the burner [13–17] or modify the flame shape [18, 19]. Heat losses to the burner are also known to alter the flame shape and its frequency response to flow perturbations [20–22], but they are more difficult to control.

Due to its high diffusivity and high reactivity compared to hydrocarbon fuels, hydrogen is often considered to modify the flame dynamics and control thermo-acoustic instabilities [23–25]. Indlekofer *et al.* [26] recently reported that addition of hydrogen substantially changes the dynamics of combustion instabilities coupled by azimuthal modes in a pressurized annular combustor. In a fully premixed H2/air model gas turbine combustor equipped with a mesoscale multinozzle array, Lee and Kim [27] found that self-sustained combustion instabilities are preferentially coupled to high eigenmodes of the combustor while with CH4/air mixtures combustion oscillations are merely coupled to the

*Corresponding author: thierry.schuller@imft.fr

first longitudinal mode of the system for the same range of operating conditions.

In a fully premixed combustor operated at a constant bulk air flowrate, Kim *et al.* [28] showed that a swirling lean methane/air V-flame bifurcates to an envelope M-flame when the equivalence ratio of the mixture increases or when at constant global equivalence ratio, the hydrogen concentration in the combustible mixture is augmented. They attribute these changes to an increased flame speed and showed that the V-flame first shortens and then switches to an M-flame for high hydrogen concentrations. The FTF of these flames were determined and the authors showed that the results could be scaled with a Strouhal number based on a flame length and a convective velocity deduced from the FTF phase lag [29]. In an analysis of the response of premixed non swirling $CH_4/H_2$ air turbulent M-flames, Aesoy *et al.* [30] also observed an increase in the cut-off frequency of the FTF for increasing hydrogen concentration. Their measurements also include the case of H2/air mixtures and their results could be scaled as a function of a Strouhal number based on the bulk flow velocity and a flame length. Additionally, modulations in the form of peaks and troughs in the gain and the phase were also identified and were shown to be caused by the interaction of two different flow disturbances, acoustic and convective, originating upstream of the flame. In an analysis of the response of premixed CH4/H2 air flame to acoustic disturbances, Yilmaz *et al.* [31] observed a significant increase in flame base coupling and flame compaction with increasing hydrogen concentration.

The alternative studied here is to operate at constant thermal power and change the heat release distribution in the reaction region with minimal alteration of the flame shape. Two injection strategies are considered for this purpose. In the first one, designated as MH, hydrogen is premixed with methane as in [28, 30]. In the second one, designated as PH, a pilot hydrogen jet is used. In this latter case, Hussain *et al.* [32] found that small hydrogen jets injected radially outward at the base of the bluff body where the flame is anchored considerably reduces heat release rate oscillations of a non-swirling methane/air flame at the forcing frequencies 30 and 255 Hz for all perturbation levels tested. In their experiments the heat release rate is deduced from the $OH^*$ emission intensity but the level of premixing of hydrogen with the main methane/air combustible mixture is not characterized.

The impact of hydrogen injection scheme on the flame response was so far not explored. The objective of this study is to compare the acoustic response of hydrogen enriched swirled flames by either premixing hydrogen with a main methane/air mixture or by pilot hydrogen injection. The motivation is to determine the best way to lower their receptivity to flowrate disturbances without substantial alteration of the global flow and flame topologies. It will be shown that these injection strategies lead to drastically different FTF/FDF. For this purpose, the acoustic response of swirling V-flames are determined experimentally for both hydrogen injection schemes and for increasing concentrations of hydrogen. Results for the FTF/FDF are then interpreted in terms of heat release rate redistribution through the reaction zone to decipher the mechanisms associated to the receptivity of these flame to incident flow perturbations.

Experiments are carried with the setup presented in section 2. The structure of the flames obtained with the two hydrogen injection schemes is analyzed in section 3. Their describing functions is examined in section 4 before scrutinizing their response at two distinct forcing frequencies in section 5 to unveil the governing mechanisms associated to H2 addition by premixing and pilot injections. A theoretical analysis is finally undertaken in section 6 to support the observations made.

## 2. Setup and diagnostics

Experiments are conducted with the MIRADAS setup described in [33] and shown in Fig. 1. Only the main components are recalled here.

A methane and air mixture is injected at the bottom and goes through a honeycomb and a converging section, where the flow is laminar. It then flows through a radial swirler with vanes at $15^o$ and is injected inside the combustion chamber by an annular channel with $2r_1 = 6$ mm internal diameter and $2r_2 = 12$ mm external diameter. Hydrogen can be fully premixed with the main mixture (MH cases) or conveyed through a tube of 4 mm internal diameter and 1 mm thickness set on the burner axis (PH cases). The top of the central injection tube protrudes by 1.25 mm from the outlet section of the annular channel conveying the swirled main combustible mixture. The flame tube of 46 mm inner diameter made of quartz provides an optical access to the flame region. Finally, the bottom of the plenum is fitted with a loudspeaker connected to an Hifi amplifier to generate harmonic flowrate modulations with frequency $f$ in the main mixture.

Figure 2 shows the two tested hydrogen injection schemes. In the MH strategy, hydrogen is premixed with the methane air mixture in the annular channel. There is in this case no flow through the central tube. In

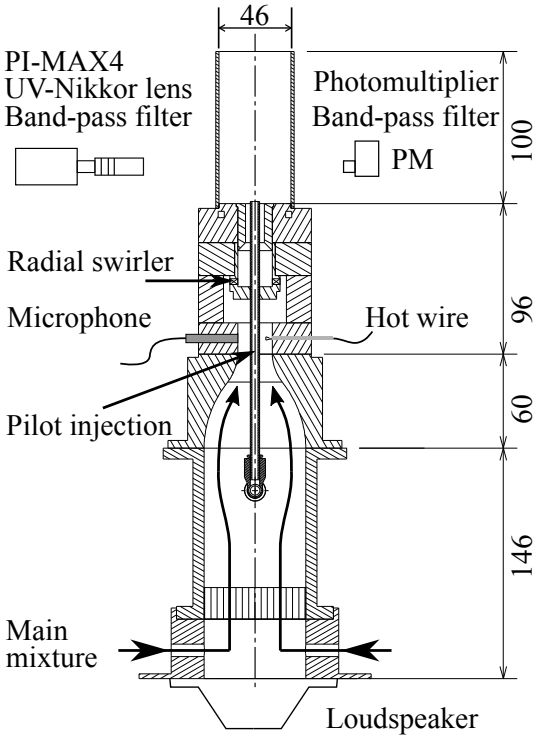


Figure 1: MIRADAS experimental setup. Main dimensions are indicated in millimeters.

the PH strategy, hydrogen is introduced through the pilot tube and the flow in the annular channel is a methane air mixture.

The convergent outlet in Fig. 1 is fitted with a hot wire probe and a wall flush mounted microphone M1. The velocity and acoustic pressure signals are used to reconstruct the acoustic velocity at the burner outlet with the procedure described in [33, 34]. The chemiluminescence is recorded by a photomultiplier equipped with ±10 nm narrow band filters centered on the $CH^*$ ($\lambda$ = 430 nm) and $OH^*$ ($\lambda$ = 308 nm) peak emissions collecting the light emission $I$ from the entire flame. These signals are used in combination with a model of the flame and flow responses to the acoustic excitation to reconstruct the heat release rate disturbances as described in Appendix A.

A PIMAX-4 intensified CCD camera equipped with a 105 mm Nikon Rayfact PF10545MF-UV lens is also used to record long exposure time flame images and phase conditional averages with respect to the forcing signal triggering the Hifi amplifier. The same type of filters as the ones used in front of the photomultiplier are put in front of the CCD camera to select the $OH^*$ or $CH^*$ intensity.

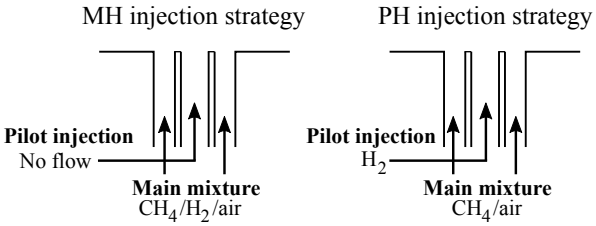


Figure 2: MH injection strategy with $H_2$ premixed within the main combustible CH4/air mixture. PH injection strategy, with $H_2$ injected pure through the central lance.

A premixed methane/air flame with equivalence $\phi$ = 0.8 and bulk velocity $u_0$ = 18 m/s serves as a reference. These conditions are obtained at the outlet of the annular channel with $T_u$ = 293 K and $p_u$ = 1 atm. The corresponding thermal power is $\dot{Q}$ = 3.9 kW. When increasing the hydrogen content, only the $CH_4$ and $H_2$ mass flowrates are modified keeping the thermal power and air flow rate constant. This leads to a small shift of equivalence ratio and bulk velocity in the annular channel. For the highest hydrogen content, the equivalence ratio reduces to $\phi$ = 0.78 and change of $u_0$ is less than 0.3 m/s. One may thus safely assume that all flames investigated in this work feature the same equivalence ratio and same bulk velocity in the annular channel [33].

## 3. Analysis of the flame structure

The analysis starts by comparing mean flame images collected with $CH^*$ and $OH^*$ filters.

Six cases are considered with different hydrogen contents for the two injection schemes, while keeping the total power of the flame constant. The reference flame, labelled Ref, is obtained for a methane and air mixture. For the premixed methane/hydrogen and air cases, two conditions are considered with 4% and 10% of the thermal power from hydrogen, respectively labelled MH4 and MH10. For hydrogen pilot injection, three conditions are tested with 2%, 4% and 10% of the total thermal power from hydrogen, respectively labelled PH2, PH4 and PH10 and corresponding to the molar fractions $X_{H_2}$ = 9%, 12% and 27% in the $CH_4/H_2$ fuel blend.

The results are presented in Fig. 3 where the left half of the flame corresponds to $CH^*$ and the right half to $OH^*$ emission intensity distributions. Camera settings are the same for all cases explored and repeatability of the results was verified over several independent runs, typically five. First, the increase in hydrogen content leads to a shortening of the flame, which is consistent with the larger flame speed of hydrogen enriched mixtures versus pure methane as already described in [28].

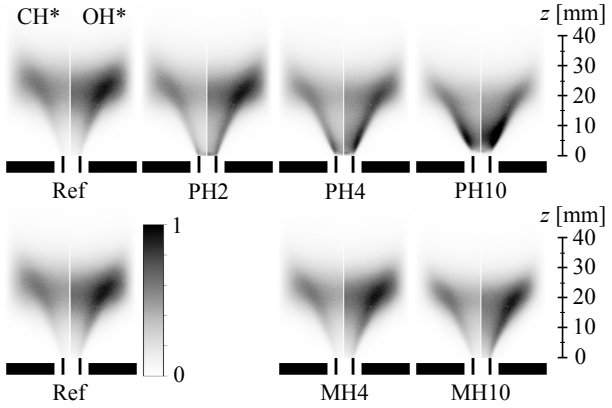


Figure 3: Influence of injection strategy (PH versus MH) and hydrogen content (in % of the total thermal power) on the mean flame structure determined from $CH^*$ and $OH^*$ emissions. The gray scale is in these images the same for all injection strategies and a given radical.

The overall flame shape is very similar using $CH^*$ or $OH^*$ emissions. Flame heights determined with the Otsu algorithm [35] applied to $CH^*$ and $OH^*$ images are synthesized in Tab. 1.

For MH cases corresponding to the second row in Fig. 3, the $OH^*$ signal is relatively uniformly spatially distributed along the reaction layer and the OH* intensity increases more than the $CH^*$ intensity as the hydrogen content increases in the combustible mixture. Due to the V-shape flame structure and rotational symmetry, the $OH^*$ or $CH^*$ intensity collected by the photomultiplier mainly originates from the top region of the flame in the Ref and MH cases.

For the PH cases shown in the top row in Fig. 3, pilot hydrogen injection strongly modifies the $OH^*$ and $CH^*$ intensities, which cannot be considered anymore spatially uniform along the flame. For PH2 and PH4, the $OH^*$ and $CH^*$ intensity levels at the flame base are comparable to those reached at the flame tip. For PH10, the $OH^*$ and $CH^*$ intensities now reach higher levels near the flame base than close to the flame tip. This is consistent with the region where one would expect that hydrogen oxydation occurs. The main difference with the fully premixing strategy is that the $OH^*$ and $CH^*$ intensities are much higher close to the flame base for pilot hydrogen injection. As a consequence, the contribution from the flame base to the total $OH^*$ or $CH^*$ light emission from the flame increases with the hydrogen flowrate injected in the pilot tube.

The main conclusion is that the MH and PH flames share the same power and same shape, but feature different distributions of the light intensity along the reaction layers, which is rebalanced towards the flame bottom for the PH cases.

Table 1: Flame height $H$ determined with the $CH^*$ and $OH^*$ emission intensities.

| $H$ [mm] | Ref | MH4 | MH10 | PH2 | PH4 | PH10 |
|---|---|---|---|---|---|---|
| $CH^*$ | 37 | 35 | 32 | 36 | 34 | 30 |
| $OH^*$ | 38 | 36 | 33 | 37 | 35 | 31 |

## 4. Flame Describing Functions

In this study the addition of hydrogen to a methane/air mixture with different injection schemes questions the methodology for the determination of heat release rate fluctuations. In the case of lean premixed flames powered by a single hydrocarbon fuel, heat release rate fluctuations are proportional to $OH^*$ or $CH^*$ emission intensity fluctuations [36]. But as pilot fuel injection leads to unperfect mixing of the reactants at the burner outlet, it is worth exploring how the link between heat release rate disturbances and the flame chemiluminescence signal is altered. This problem is examined in Appendix A with a series of additional experiments. Only the main conclusions are summarized here.

For the cases considered in this study, results obtained by making use of the $CH^*$ or $OH^*$ light intensities are identical independently of the strategy used to inject hydrogen. It is shown that for a fixed velocity modulation level $\tilde{u}_0/\overline{u}_0$ at the annular channel outlet, harmonic heat release rate $\widetilde{\dot{Q}}$ and $CH^*$ intensity $\tilde{I}$ disturbances are linked by:

$$\frac{\widetilde{\dot{Q}}}{\overline{\dot{Q}}} = \frac{\tilde{I}}{\overline{I}} + \beta Y_{H2} \frac{\tilde{u}_0}{\overline{u}_0} \tag{1}$$

where the coefficient $\beta$ is equal to zero for the premixed MH injection scheme and is given by Tab. 2 for the pilot PH hydrogen injection scheme.

Table 2: Parameters appearing in the relationship $I = k\dot{Q}\phi^{\beta}$ between the $CH^*$ intensity $I$, equivalence ratio $\phi$ and heat release rate $\dot{Q}$. The hydrogen mass fraction $Y_{H_2}$ in the methane/hydrogen fuel blend is also indicated.

| | Ref | MH10 | PH2 | PH4 | PH10 |
|---|---|---|---|---|---|
| k [V/kW] | 2.32 | 2.00 | 2.12 | 2.07 | 1.91 |
| $\beta$ | 3.63 | 3.13 | 3.31 | 3.19 | 2.82 |
| $Y_{H_2}$ | 0.00 | 0.04 | 0.01 | 0.02 | 0.04 |

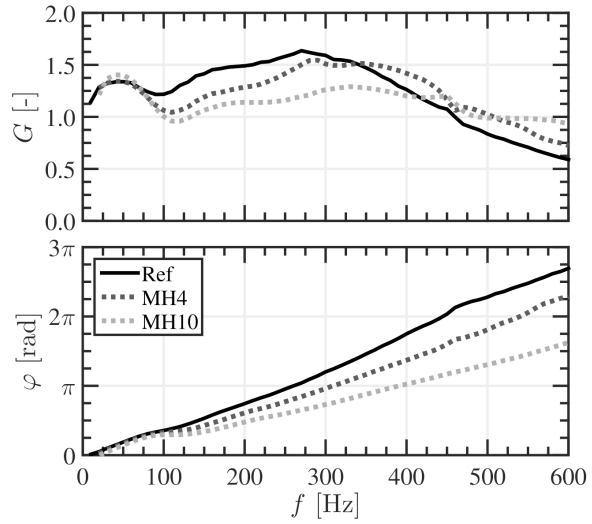


Figure 4: FDFs for premixed cases (MH). Pulsation level $\tilde{u}_0/\overline{u}_0 = 0.3$.

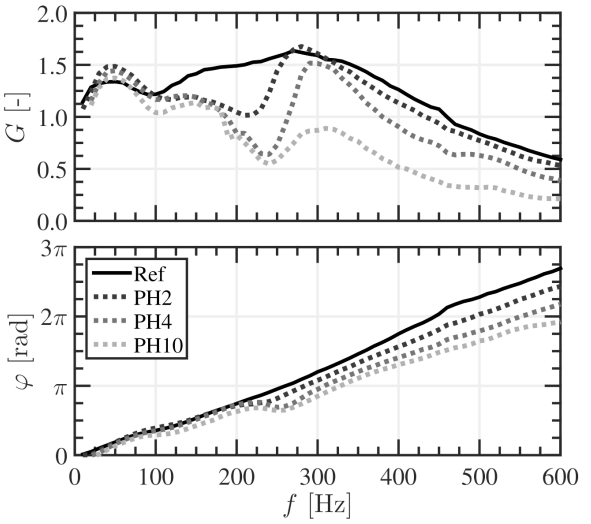


Figure 5: FDFs for piloted cases (PH). Pulsation level $\tilde{u}_0/\overline{u}_0 = 0.3$.

Flames are submitted to harmonic acoustic excitations. The velocity modulation level $\tilde{u}_0/\overline{u}_0 = 0.10$, 0.30 or 0.60 at the annular channel outlet is kept constant for all forcing frequencies with the method described in [33]. The flame response is deduced from a two step procedure. First, the cross $S_{uI}$ and power $S_{uu}$ spectral densities of the light intensity $I$ from $CH^*$ radicals and the reconstructed velocity signal $u_0$ at the annular channel outlet is determined:

$$\frac{\tilde{I}}{\overline{I}} = \mathrm{FDF}_I \frac{\tilde{u}_0}{\overline{u}_0} \tag{2}$$

where $\tilde{u}_0$ and $\tilde{I}$ denote the Fourier components of the signals at the harmonic modulation frequency $f$ and $\overline{u}_0$ and $\overline{I}$ correspond to their mean values.

Table 2 indicates that the product $\beta Y_{H_2}$ remains small in these experiments due to the small quantities of hydrogen injected in the system, meaning that the second term in the right hand side in Eq. (1) appears as a slight correction of the first term. As a consequence, the impact of equivalence ratio disturbances resulting from pilot hydrogen injection remains small compared to flow rate disturbances in this setup. This would not be the case for higher mass flow rates of hydrogen injected in the pilot lance.

For the PH10 case submitted to both flowrate and equivalence ratio disturbances, the light intensity signal is corrected with Eq. (1) to reconstruct the corresponding heat release rate fluctuations. Figure 20 compares the PH10 flame frequency responses determined with the $CH^*$ light intensity and with the heat release rate reconstruction. The two responses only slightly differ due to the limited impact of mixture composition disturbances as shown in Appendix A. One remarkable feature is that the gain determined with $\tilde{\dot{Q}}/\overline{\dot{Q}}$ approaches closer to unity as the forcing frequency goes to zero. The phase lag is not altered by the correction.

The FDF linking heat release rate disturbances and the velocity modulation level at the annular channel outlet are in the following all determined with:

$$\frac{\widetilde{\dot{Q}}}{\overline{\dot{Q}}} = (\mathrm{FTF}_I + \beta Y_{H_2}) \frac{\tilde{u}_0}{\overline{u}_0} = G \exp(i\varphi) \frac{\tilde{u}_0}{\overline{u}_0} \tag{3}$$

where $\beta$ is set to zero for the Ref, MH4 and MH10 cases and is given by Tab. 2 for the PH cases. Results are first presented for a pulsation level $\tilde{u}_0/\overline{u}_0 = 0.3$, which corresponds to typical limit-cycle amplitudes observed in the system during unstable operation [33].

Proceeding with premixed cases first, the FDFs of MH4 and MH10 are compared to the methane/air Ref case in Fig. 4. Below 70 Hz, there is no influence of the hydrogen content on the flame responses but past this value, both the FDF phase lag and FDF gain are affected. The phase is consistently reduced by increasing the hydrogen content for all frequencies. At 600 Hz, the FDF phase lag is close to $3\pi$ for the Ref case and drops below $2\pi$ for MH10. The FDF gain is lowered at frequencies below 450 Hz but increased above this mark for MH4 and MH10. Both of these features are attributed to the increase in flame speed and subsequent decrease in flame length [28, 30], leading to a higher cutoff frequency for the FDF gain and a reduced time lag $\tau = \varphi/(2\pi f)$ between heat release rate disturbances and flowrate perturbations at the burner outlet.

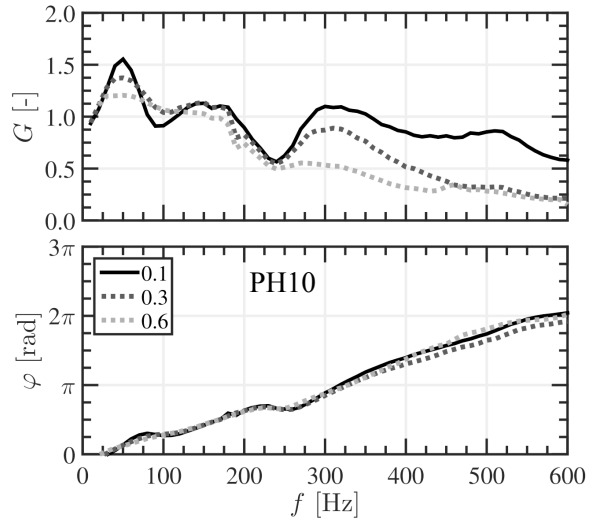


Figure 6: PH10 FDF for three pulsation levels $\tilde{u}_0/\overline{u}_0 = 0.1$, 0.3 and 0.6.

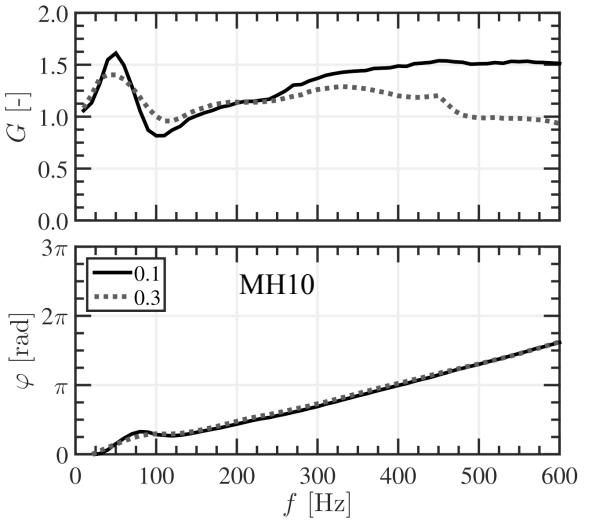


Figure 7: MH10 FDF for two pulsation levels $\tilde{u}_0/\overline{u}_0 = 0.1$ and 0.3.

It is commonly admitted that fully premixed hydrogen-enriched flames feature a broader frequency range over which they are sensitive to thermo-acoustic instabilities compared to operation without hydrogen [28]. To illustrate this feature, one may compare the cut-off frequency $f_c$, defined here as the frequency above which the FTF gain drops below unity ($G(f_c) < 1$), from the Ref case at $f_c = 450$ Hz and the MH10 case at $f_c = 600$ Hz.

The FDFs for pilot injection PH2, PH4 and PH10 are presented in Fig. 5. First regarding the FDF phase lag, there is a reduction concomitant with the increase in hydrogen content, but this time the values start departing from the Ref case at around 240 Hz. Interestingly, the FDF phase lag at 600 Hz for the pilot injection PH10 reaches a value $\varphi = 3\pi/2$ close to that reached by the premixed MH10 case shown in Fig. 4.

Regarding the FDF gain, pilot hydrogen leads to an overall reduction at almost all frequencies. The gain reduction also increases with the hydrogen content. This means that unlike the premixed cases, the decrease in flame length does not lead to an overall increase in the cutoff frequency $f_c$ of the flame response. The reverse trend is observed indicating that a phenomenon specific to the piloting has affected the FDF. Using the same definition for the gain cut-off frequency as for the premixed cases, i.e. $G(f) < 1$ for $f > f_c$, one finds that it drops from $f_c = 460$ Hz for the Ref case to $f_c \simeq 300$ Hz for PH10. This value has to be compared to $f_c = 600$ Hz found for the cut-off frequency of the premixed case MH10 with the same thermal power originating from hydrogen as PH10. It is also worth noting that MH10 and PH10 share the same flame height as indicated in Tab. 1.

In the preceding experiments the amplitude of the incoming flow disturbances was kept constant and fixed to $\tilde{u}_0/\overline{u}_0 = 0.3$. Effects of the forcing level are now explored for MH10 and PH10 in Figs. 6 and Figs. 7 for the pilot and fully premixed injection strategies respectively. With pilot injection, a reduction of the FDF gain above $f > 240$ Hz is observed at small and large perturbation levels and this gain reduction increases with the perturbation level $\tilde{u}_0/\overline{u}_0 = 0.1$, 0.3 and 0.6 in Fig. 6. In the fully premixed case, one may again notice the large frequency range over which the FDF gain exceeds unity in Fig. 7. For velocity disturbances as low as $\tilde{u}_0/\overline{u}_0 = 0.1$, the cut-off frequency largely exceeds $f_c > 600$ Hz in the premixed case compared to $f_c = 400$ Hz for pilot injection and the same perturbation level in Fig. 6. The FDF gain of the premixed flame also drops for increased modulation amplitudes above $f > 240$ Hz, but still remains above unity for frequencies as high as 600 Hz and $\tilde{u}_0/\overline{u}_0 = 0.3$. Larger modulations levels $\tilde{u}_0/\overline{u}_0 > 0.3$ could not be explored with this hydrogen content and the fully premixed strategy due to a progressive heat up of the central fuel lance as the flame periodically sweeps back and forth along the metal during the forcing cycle. This cyclic motion of the flame base led to a further increase of the metal temperature with a flame further protruding inside the injector leading finally to flashback. With the pilot injection strategy, modulation levels as high as $\tilde{u}_0/\overline{u}_0 = 0.6$ could be reached without significant heat up of the central fuel lance.

It will be shown in the following section that these different behaviors are the consequence of the redistribution of heat release rate along the flame arms towards the root of the flame.

## 5. Spatial analysis of the flame response

Two frequencies of interest are identified for a spatial analysis of the flame response. The first one $f = 240$ Hz corresponds to a dip in the FDF gain for PH cases as shown in Fig. 5, a situation where the FDF phase lag deviates from the Ref case for increasing hydrogen contents. The second one $f = 590$ Hz is selected because the FDF gain evolves in opposite directions with respect to the Ref case for PH (Fig. 5) and MH (Fig. 4). Incidentally, it also corresponds to a self-excited combustion instability that is triggered for a longer chamber and a longer plenum, but this point is not discussed here.

Phase conditional averaged images of the flame response were collected at these forcing frequencies and a pulsation level $\tilde{u}_0/\overline{u}_0 = 0.3$. For each forcing frequency, $N = 12$ phases describe a full oscillation cycle. The dynamics of the flame is illustrated in Fig. 8 for the Ref case with a narrow-band interferometric filter centered on CH* emission. Only four phases are represented in the cycle. The indication on the top left corner in the images stands for the phase lag with respect to the harmonic velocity modulation $\tilde{u}_0$ at frequency $f = 240$ Hz at the annular channel outlet. A two axes coordinate system $(r, z)$ is defined. The origin lies on the symmetry axis of the burner at the outlet of the central fuel lance.

To ease interpretation of these images, a principal harmonic analysis of the CH* intensity distribution along the axial direction is carried out. The procedure is as follows. For each of the $N = 12$ images, the cumulated intensity distribution along the $z$-axis is first determined by summing all pixel values along the radial $r$-axis. A discrete Fourier transform of these signals over the $N = 12$ phases in the forcing cycle is then performed. The principal harmonic analysis only retains the main components of the nonlinear flame response at zero frequency $f_0 = 0$ and at the forcing frequency $f$ by assuming that all harmonics at $nf$, with $n \geq 2$ only weakly contribute to this response. The discrete inverse Fourier transform over $N$ points is then applied to this truncated complex signal to get the following real signal:

$$I_r(z_j; k) = \overline{I}_r(z_j) + I_r^e(z_j) \cos\left(\frac{2\pi k}{N} + \beta_k\right) \tag{4}$$

where $z_j$ denotes the position along the $z$-axis, $k$ is the phase in the forcing cycle and $\beta_k$ is a phase lag. In this

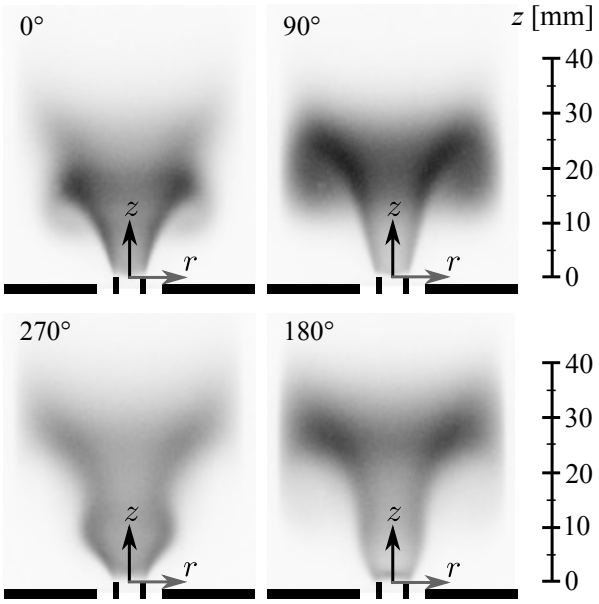


Figure 8: Phase-averaged CH* emissions for the methane premixed case (Ref case). $\tilde{u}_0/\overline{u}_0 = 0.3$, $f = 240$ Hz.

expression $\overline{I}_r(z_j)$ is the temporal average of the original nonlinear signal and $I_r^e(z_j)$ is the envelope of the harmonic component at the forcing frequency $f$ deduced from an Hilbert transform.

Summation of $\overline{I}_r(z_j)$ over the axial direction yields the global mean intensity averaged over an oscillation cycle as would be detected by a photomultiplier:

$$\overline{I} = \sum_j \overline{I}_r(z_j) \tag{5}$$

### 5.1. Analysis at 240 Hz

The methodology described above is used to determine the axial distributions of $\overline{I}_r$ and $I_r^e$ along the $z$-axis. These distributions are plotted in Figs. 9 and 10 for the MH and PH cases, respectively, for flames forced at $f = 240$ Hz and $\tilde{u}_0/\overline{u}_0 = 0.3$.

The normalized time-averaged magnitude $\overline{I}_r(z)/\overline{I}$ plotted in Figs. 9a and 10a is used to determine the regions in the flame that contribute the most to the global CH* intensity. Both figures show similar trends with the maximum moving upstream as the fraction of hydrogen increases. In Fig. 9a the maximum shifts from $z = 26$ mm for the Ref case to $z = 18$ mm for MH10. This maximum lies always in the upper region of the flame as confirmed by the data gathered for the flame height synthesized in Tab. 1. In the mean time, the flame height is reduced from $H = 39$ mm for the Ref case to

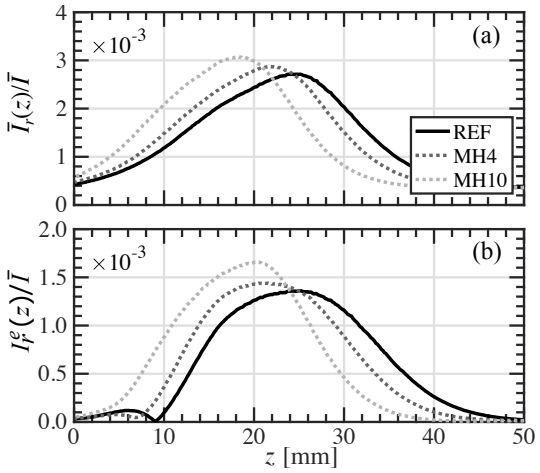


Figure 9: MH cases versus Ref at $f = 240$ Hz: longitudinal evolution of the cross-stream heat release rate response. a) Normalized time-averaged relative magnitude $\bar{I}_r(z)/\bar{I}$. b) Normalized harmonic fluctuation envelope $I_r^e(z)/\bar{I}$ at frequency $f$.

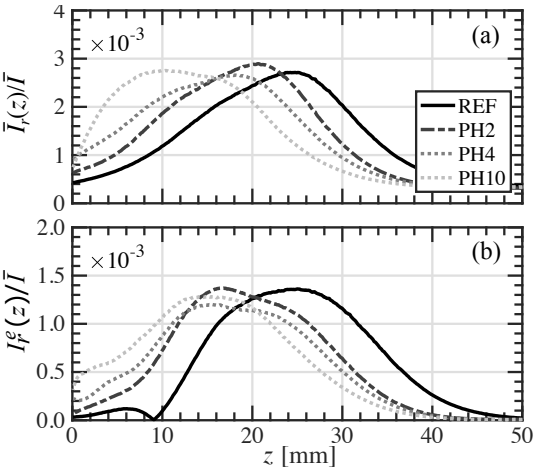


Figure 10: PH cases versus Ref at $f = 240$ Hz: longitudinal evolution of the cross-stream averaged heat release rate response. a) Normalized time-averaged relative magnitude $\bar{I}_r(z)/\bar{I}$. b) Normalized harmonic fluctuation envelope $I_r^e(z)/\bar{I}$ at frequency $f$.

$H = 34$ mm for MH10. As a consequence, the shift observed in light intensity distribution for the MH flames is partly due to the shortening of the premixed flames as the hydrogen content increases. In Fig. 10a, a bigger shift of the region contributing the most to the global heat release rate towards the burner outlet is observed as the hydrogen content increases with pilot injection. This is particularly striking for PH10 with a maximum that reaches a plateau centered around $z = 10$ mm and spreads between 4 and 16 mm. Table 1 indicates that this shift is also partly due to the shortening of the flame as already observed for the MH cases. Note that the flame heights for PH10 and MH10 are very close in Tab. 1. But the increased reactivity at the flame root due to hydrogen pilot injection is the main mechanism responsible for this redistribution of the heat release rate towards the flame root (see PH10 in Fig. 3).

The normalized harmonic fluctuation envelopes $\tilde{I}_r^e(z)/\bar{I}$ are plotted in Figs. 9b and 10b with, again, similar features for the two injection strategies. For all cases, the maximum of fluctuation moves upstream when increasing the amount of hydrogen injected in the burner. These two features are related to the flame shortening as the hydrogen concentration in the flow increases. One may however note that close to the burner outlet, between $0 \leq z \leq 10$ mm, the redistribution of light intensity fluctuations towards upstream is much more pronounced in Fig. 10b for the hydrogen pilot injection PH cases than in Fig. 9a for the hydrogen enriched MH mixtures.

The last quantity plotted in Fig. 11 corresponds to the axial evolution of the projection of $\tilde{I}_r(z)$ on $\tilde{I}$:

$$p(z) = \frac{|\tilde{I}_r(z)|}{|\tilde{I}|} \cos\left[\angle\left(\tilde{I}_r(z), \tilde{I}\right)\right] \tag{6}$$

Positive values of $p(z)$ indicate that at location $z$, the contribution of the CH* intensity fluctuation $\tilde{I}_{rz}$ has an absolute phase difference with the global fluctuation $\tilde{I}$ lower than $\pi/2$. In other words, the CH* intensity at this location contributes positively towards the global response $\tilde{I}$. Conversely, negative values of $p(z)$ indicate a local contribution that is 'pulling backwards' the global response. The magnitude of $p(z)$ indicates how

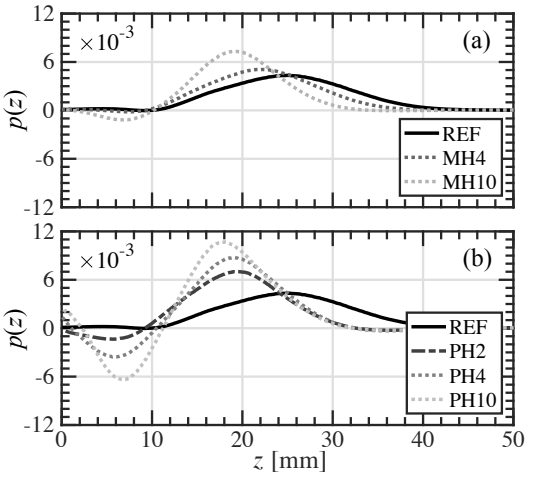


Figure 11: Projection $p(z)$ of $\tilde{I}_r(z)$ on $\tilde{I}$ for (a) the premixed and (b) the pilot injection strategies for flames forced at $f = 240$ Hz.

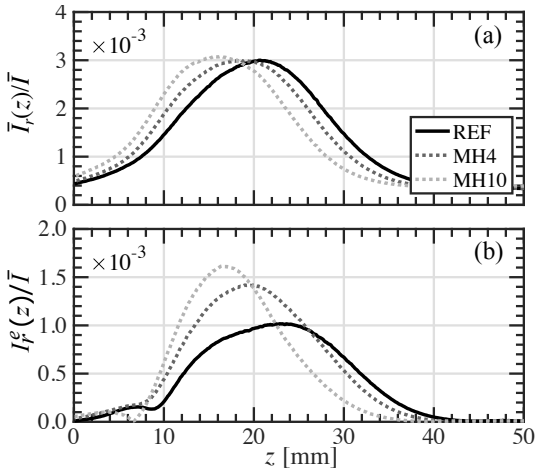


Figure 12: MH cases versus Ref at $f = 590$ Hz: longitudinal evolution of the cross-stream heat release rate response. a) Normalized time-averaged relative magnitude $\bar{I}_r(z)/\bar{I}$. b) Normalized harmonic fluctuation envelope $I_r^e(z)/\bar{I}$ at frequency $f$.

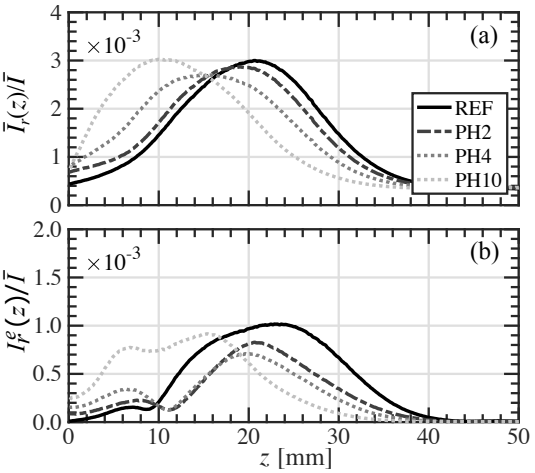


Figure 13: PH cases versus Ref at $f = 590$ Hz: longitudinal evolution of the cross-stream heat release rate response. a) Normalized time-averaged relative magnitude $\bar{I}_r(z)/\bar{I}$. b) Normalized harmonic fluctuation envelope $I_r^e(z)/\bar{I}$ at frequency $f$.

strong the local contribution is with respect to the global response.

For the reference case plotted in Figs. 11a-b, $p(z)$ is positive all along the flame, despite a small wiggle around $z = 10$ mm. Examining first the premixed MH cases in Fig. 11a, the increase in hydrogen content moves the maximum upstream with a simultaneous increase in magnitude. This increase is partly compensated by a small region where $p(z) < 0$ around $z = 10$ mm, resulting in an overall slight reduction in the FDF gain for MH4 and M10 compared to the Ref case, as seen in Fig. 4 at $f = 240$ Hz.

For all the pilot cases shown in Fig. 11b, the addition of hydrogen moves the location of the maximum about 8 mm upstream, almost independently of the hydrogen fraction injected. The magnitude of this maximum also increases with the hydrogen content. More interestingly, a region of negative values is formed between $z = 2$ mm and $z = 12$ mm, with a magnitude increasing with the hydrogen content. This indicates that it is the dynamics at the flame base that is driving the global reduction of the FDF gain observed for the PH cases in Fig. 5 at $f = 240$ Hz. Heat release rate fluctuations originating from the flame root region are in phase opposition with those originating closer to the flame tip leading to a reduction of the global heat release rate fluctuation $\tilde{I}$. Since the forcing level is kept constant this also leads to the drastic drop of the FDF gain observed at this frequency in Fig. 5.

As a consequence, the origin of the drop of the FDF gain at $f = 240$ Hz is due to a compensation of heat release rate oscillations originating from the flame tip by heat release rate oscillations originating from the flame base that fluctuate in phase opposition with respect to the flame tip. Due to the V-shape structure of the reaction layer and the rotational symmetry of the flame, the flame surface area close to the flame tip is much larger than at the flame base. By premixing H2 with the main mixture, the reaction rate, identified by the $CH^*$ or $OH^*$ emission intensities, increases but remains roughly uniformly distributed along the flame sheet indicating that the burning rate remains also roughly constant along the flame sheet. The heat release rate being proportional to the product of the burning rate by the flame surface area, this explains why heat release rate fluctuations originating from the flame base remain small in Fig. 11a for the MH premixed injection strategy. In contrast, these fluctuations are amplified in Fig. 11b for the PH pilot injection strategy due to the large increase of the reactivity, i.e. the burning rate, at the flame base compared to the flame tip. It is now worth exploring what is happening at a higher forcing frequency.

### *5.2. Analysis at 590 Hz*

The same analysis is repeated for a forcing frequency $f = 590$ Hz, where the FTF of the MH and PH cases show opposite trends with respect to the Ref case in Figs. 4 and 5.

Results for the premixed cases are presented in Fig. 12. As expected, the maximum of heat release rate in Fig. 12a moves slightly upstream as the flame shortens due to the higher burning velocity with the in-

creasing content of hydrogen in the combustible mixture. The mean $\bar{I}_r(z)/\bar{I}$ and envelope $\tilde{I}_r(z)/\bar{I}$ profiles shown in Fig. 12a and b respectively being very similar to the ones plotted in Fig. 9a and b when the flame was forced at $f = 240$ Hz, one expects the response of these flames forced at $f = 590$ Hz to be very similar to that at $f = 240$ Hz. The main difference is that the wave like pattern in the projection $p(z)$ takes place over a shorter scale and features more undulations at $f = 590$ Hz in Fig. 14 than in Fig. 11 when the flame was forced at $f = 240$ Hz. Overall, Fig. 14a indicates that $p(z)$ remains largely positive along the flame reaction layer from $z = 0$ to the flame tip and reaches higher levels as the hydrogen concentration increases in the injected fuel. This explains why the FTF gain for MH flames slightly increases at $f = 590$ Hz with the hydrogen content in Fig. 4.

Results with pilot injection presented in Fig. 13 show again a different behavior. As for 240 Hz, the increased reactivity at the flame base and the shortening of the flame shifts the maximum of $\bar{I}_r(z)$ more upstream in Fig. 13a for pilot injection compared to Fig. 12a for premixed injection. Regarding the normalized envelope $I_r^e(z)$ shown in Fig. 13b, there is a small reduction of the maximum for hydrogen enriched flames compared to the Ref case, but the main consequence of hydrogen addition is much larger fluctuations close the burner outlet compared to the Ref case and the MH premixed injection strategies. For $0 \leq z \leq 12$ mm, the fluctuation level again rapidly increases in Fig. 13b with the hydrogen content as already noticed at 240 Hz for hydrogen pilot injection in Fig. 10b.

Figure 14b indicates that for cases PH2, PH4 and PH10, the reduction in the overall heat release rate fluctuation for pilot injection is caused by an increased magnitude of the wavy pattern near the burner outlet when the hydrogen flowrate in the pilot lance is increased. This is particularly striking for PH10 that shows an alternating pattern with positive and negative contributions to the global heat release rate oscillation. One first identifies a large positive peak at $z = 4$ mm, followed by a deep drop with a negative minimum reached at $z = 10$ mm before it re-increases again to reach another maximum at $z = 18$ mm and finally the oscillation vanishes by crossing again zero close to the flame tip. These interferences already identified in Fig. 11 for the PH flames forced at $f = 240$ Hz are amplified here and are responsible for the strong attenuation of the global $CH^*$ intensity fluctuation $\tilde{I}$ and the low FDF gain values seen in Fig. 5 at 590 Hz.

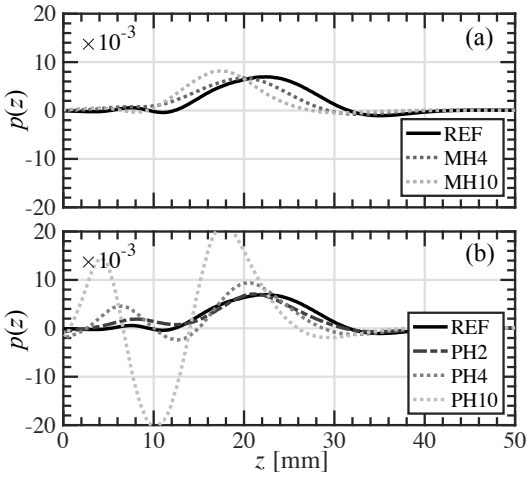


Figure 14: Projection $p(z)$ of $\tilde{I}_r(z)$ on $\tilde{I}$ for (a) the premixed and (b) the pilot injection strategies for flames forced at $f = 590$ Hz.

## 6. Theoretical analysis

To sump up, a wavy pattern with alternating regions of positive and negative contributions to the global heat release rate fluctuation has been identified in the distribution of $p(z)$ along the axial coordinate $z$. This pattern is discernable at the two forcing frequencies $f = 240$ Hz and $f = 590$ Hz, for the premixed methane/air Ref case, the premixed MH cases and the pilot injection PH cases in Figs. 11 and 14. The main difference between the response of the premixed and pilot cases is that fluctuations near the flame base remain small compared to those at the flame tip for all the premixed injection cases explored. For the pilot cases, heat release rate fluctuations at the flame base drastically increase with the hydrogen content injected in the system. These wavy patterns highlight interferences taking place between heat release rate fluctuations produced at different locations along the reaction layer.

Wrinkles along reaction layers are a well known feature of the response of fully premixed flame sheets inclined with respect to the mean flow and submitted to axial flowrate modulations [7, 8, 11, 37]. One now looks into how effects of swirl and hydrogen enrichment may eventually alter this response.

### *6.1. Effects of swirl*

Considering first effects of swirl. When a swirled burner is submitted to acoustic disturbances, azimuthal inertial waves downstream the swirler are produced in addition to the acoustic excitation [14, 38, 39]. The acoustic and inertial waves travel at different speeds inside the burner and were shown to lead to radial ve-

locity fluctuations at the burner outlet that wrinkle the flame sheet in addition to axial disturbances [40, 41]. The main consequence for a swirled flame anchored on a central bluff body is that its transfer function features a succession of peaks separated by valleys at specific frequencies [14, 16, 42, 43]. The frequency at which these destructive interferences take place depends on the bulk flow velocity and the distance $l_s$ between the swirler and the burner outlet [14]. The frequency $f_m$ of the first valley corresponds to a situation where axial and azimuthal velocity disturbances are out of phase by $\Delta\varphi_{u_z-u_\theta} = \pi$ at the burner outlet [42–44]. When this condition is met, oscillations of the flame angle at the flame anchoring region are the largest due to large oscillations of the swirl level. Heat release rate fluctuations in the lower region of the flame are in this case out of phase with fluctuations in the upper region of the flame resulting in a global cancellation and a reduction of the gain of the flame transfer function at the frequency $f_m$.

The reason why this gain reduction is not clearly seen for the premixed MH cases plotted in Fig. 4 is that the swirl level remains relatively weak in the configurations explored. Numerical flow simulations carried out in [45] yield a Swirl number value:

$$S = \frac{\int_{r_1}^{r_2} \overline{u}_z \overline{u}_\theta r^2 dr}{r_2 \int_{r_1}^{r_2} \overline{u}_z^2 r dr} = 0.35 \tag{7}$$

at the burner outlet $z = 0$, where $\overline{u}_z$ and $\overline{u}_\theta$ denote the time averaged values of the axial and azimuthal velocity components respectively. For fully premixed swirled flames, it was shown that the drop of the FTF gain at frequency $f_m$ is only perceptible for a sufficiently large swirl number $S$, typically above 0.5 [16, 46]. The magnitude of the FTF gain reduction then increases with the swirl level due to larger oscillations of the flame angle at the flame base. In the present cases, the swirl level remains relatively low leading to limited swirl number oscillations and flame angle oscillations at the flame base when the flames are submitted to acoustic excitations. As a conclusion, the limited swirl level of the studied flames leads to a relatively weak influence of fluctuations of the swirl level on the response of these flames.

Another specific feature of swirled flames is that they may often be accompanied by hydrodynamic helical flow instabilities [47] taking place at frequencies independent of the acoustic forcing frequency. These structures were shown to alter the FTF gain by nonlinear interactions between the mean and perturbed flow fields for sufficiently large forcing level [48]. But in the present cases no precessing vortex core interacting with the investigated flames could be detected with the technique developed in [49]. The reason may again be attributed to the relatively low swirl level impregnated to these flames that remains below typical threshold levels at which these flow instabilities are generally observed.

It is also striking that the FDF gain of flames with pilot hydrogen regularly drops in Fig. 5 by increasing the hydrogen content. This reduction is observed over almost the entire frequency range and is not limited to only well specific forcing frequencies. Effects of swirl oscillations and hydrodynamic instabilities associated to swirled flows are discarded in the following analysis, not because they are unimportant, but this approximation is used to better emphasize another mechanism causing a gain reduction which is specific to the response of flames with pilot hydrogen and which is independent of the forcing frequency.

### *6.2. Effects of hydrogen injection*

One now attempts to determine why pilot hydrogen injection leads to a global reduction of the FTF gain while premixing hydrogen with the main methane/air mixture leads to more responsive flames over a wider frequency range. Due to the rotational symmetry of the flame along the $z$-axis and its V-shape structure, the fluctuations taking place at the flame base contribute less to the global heat release rate oscillation when the burning rate remains relatively uniform along the reaction layer as for the Ref and MH premixed flames. With hydrogen pilot injection, the reactivity drastically increases at the flame base compared to the flame tip leading to oscillation levels in this region comparable to those found at the flame tip. It has been shown in the preceding section that interferences between perturbations at the flame base and at the flame tip lead in this latter case to a drop of the FTF gain. It is remarkable that this mechanism is effective over a wide range of frequencies.

A low order model is derived to examine the consequences on the flame response to acoustic waves when the flame features a non uniform heat release rate distribution. The model is not intended to reproduce the FTF observed in the experiments, but aims at providing a theoretical background to support the global flame response reduction observed in the experiments for the hydrogen pilot injection cases. It is based on a kinematic description of the dynamics of a thin reaction layer submitted to acoustic disturbances by assuming that harmonic heat release rate disturbances $\widetilde{\dot{Q}}$ are given by:

$$\frac{\widetilde{\dot{Q}}}{\overline{\dot{Q}}} = \frac{\int \overline{\dot{q}} d\tilde{A}}{\int \overline{\dot{q}} d\overline{A}} \tag{8}$$

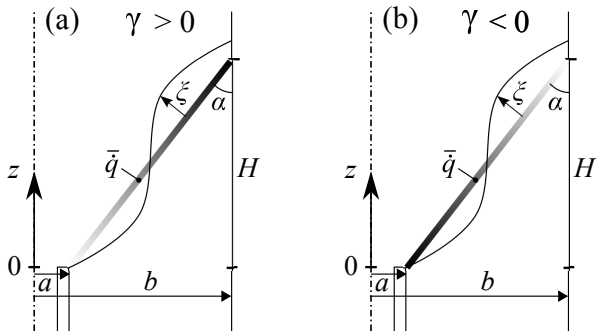


Figure 15: Geometry for the perturbed flame sheet model with a non uniform heat release rate distribution $\overline{\dot{q}}$. The two flames share the same flame surface area. (a) $\gamma > 0$: The burning intensity increases along the reaction layer. (b) $\gamma < 0$: The burning intensity drops along the reaction layer.

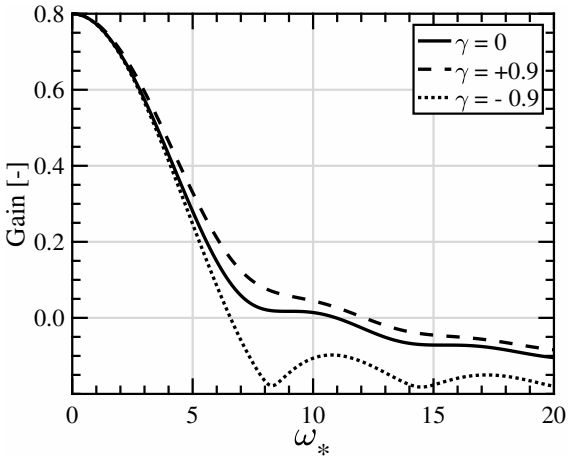


Figure 16: Gain of the FTF model with a constant burning intensity $\gamma = 0$, a burning intensity that increases along the flame arms $\gamma = +0.9$ and a burning intensity that reduces along the flame arms $\gamma = -0.9$. $a = 3$ mm, $b = 23$ mm.

In this expression, $\overline{\dot{q}}$ denotes the mean burning intensity, i.e. the mean local heat release rate per unit flame surface area. For fully premixed flames, it is often assumed that $\overline{\dot{q}} = \dot{q}_0$ remains constant along the reaction layer and one retrieves the classical relationship between heat release rate disturbances and flame surface area fluctuations: $\tilde{Q}/\overline{Q} = \tilde{A}/\overline{A}$. Equation (8) generalizes the relationship between flame surface area and heat release rate disturbances to the case of flames with a non uniform heat release distribution along the reaction layer when disturbances of the burning intensity $\dot{q}$ can be neglected compared to flame surface wrinkling. For the fully premixed flames and the pilot hydrogen enriched flames considered in this study for which equivalence ratio fluctuations were shown to be limited, this approximation is reasonable.

Figure 15 shows the geometrical configuration investigated. Two configurations are explored. They share the same flame shape, i.e. the same flame surface area and also release the same thermal power. They only differ by the way the burning intensity $\overline{\dot{q}}(z)$ is distributed along the reaction layer. In Fig. 15(a), it increases from the root to the tip, while it drops in Fig. 15(b). To simplify the problem, one assumes that $\overline{\dot{q}}(z)$ linearly changes with the distance $z$ to the flame base:

$$\overline{\dot{q}}(z) = \dot{q}_0 \frac{1}{c}\left(1 + \gamma \frac{z}{H}\right) \tag{9}$$

where $0 \leq z \leq H$, $H$ stands for the flame height and $\gamma$ is a constant parameter. When $\gamma$ is positive, respectively negative, the burning intensity increases, respectively decreases, along the reaction layer. The parameter $c = 1 + \gamma\,(a/(b+a) + (2/3)(b-a)/(b+a))$ is introduced to study flames featuring different burning intensity distributions, but sharing the same global heat release rate $\overline{Q} = \dot{q}_0 \overline{A}$ and same flame surface area $\overline{A} = \pi(b^2 - a^2)/\sin\alpha$.

When the flame is submitted to harmonic velocity modulations at the burner outlet, the resulting heat release rate disturbances may be decomposed as:

$$\frac{\widetilde{Q}}{\overline{Q}} = \frac{1}{c}\left(FTF_{\gamma=0} + \gamma FTF_{\gamma\neq 0}\right)\frac{\tilde{u}_0}{\bar{u}_0} \tag{10}$$

Expressions for $FTF_{\gamma=0}$ and $FTF_{\gamma\neq 0}$ are given in Appendix B assuming a uniform flow perturbation along the reaction layer. The same methodology can be extended to include more realistic flow perturbation models and more realistic heat release distributions along the reaction layer. Only the minimum physics is retained here to illustrate effects of a non uniform heat release rate distribution on the flame response.

Results plotted in Fig. 16 compare the FTF gain for three flames featuring the same shape and thermal power, but different heat release rate distributions along the reaction layer. Results are plotted as a function of the reduced frequency $\omega_* = (\omega H/\bar{u}_0)(1/\cos^2(\alpha))$, which has been shown to be the correct scaling factor at low frequencies [50]. The cases considered correspond to parameters set to $a = 3$ mm, i.e. the radius of the central injection tube and $b = 23$ mm, i.e. the flame tube radius. The reference is obtained for a flame with a uniform burning intensity when $\gamma$ is set to zero in Eqs. (9) and (10) [50]. This is the configuration that is considered in most kinematic models of the flame response, in which the burning rate is assumed to be constant [8]. The situation where the burning intensity

increases along the reaction layer in Fig. 15(a) mimics the distribution seen for the MH flames in Fig. 3. Results with $\gamma = +0.9$ show that the FTF gain takes always slightly higher values over the entire frequency range than the reference with a uniform burning intensity when $\gamma$ is set to zero. Figure 15(b) mimics the situation where the burning intensity drops along the reaction layer as for the PH cases in Fig. 3. For $\gamma = -0.9$ characterizing a flame with a higher burning intensity at the flame root compared to the flame tip, the FTF gain is now lower than the reference flame with a uniform heat release distribution. The same trends are observed but with reduced differences when the value for $|\gamma|$ is reduced.

This model confirms that flames featuring the same global heat release rate $\overline{\dot{Q}}$ and same height $H$, flame shape, but a higher burning intensity close to the flame tip like the premixed Ref, MH2, MH4 and MH10 cases studied herein feature larger FTF gain values over the entire frequency range than the same flames but featuring a higher burning intensity closer to the flame base like the PH4 and PH10 flames (see Fig. 2). This theoretical analysis corroborates the observations made that a redistribution of the heat release towards the bottom of the flame tends to make the flames less responsive to incoming flow perturbations.

The most obvious feature with hydrogen pilot injection being the redistribution of the mean heat release towards the flame bottom, further dynamical aspects need however to be considered to fully interpret the response of the flames with pilot hydrogen. Figure 2 shows that PH4 and PH10 flames are slightly lifted above the injector with respect the methane/air Ref case and the hydrogen premixed MH2 to MH10 flames. Figures 10 and 13 also show larger fluctuations of the flame base at $z = 0$ for the PH cases with respect to the MH cases in Figs. 9 and 12, meaning that the oscillations of the flame anchoring point probably also play some role in the response of the studied flames. Finally, it is known that wrinkles propagating along a reaction layer depend on flame stretch and flame curvature [51]. Flame anchoring dynamics and curvature effects may be enhanced with hydrogen injection due to its higher burning velocity and low Lewis number. The dynamics associated to these features were not considered in the present analysis and are left for further studies.

## 7. Conclusion

The frequency response of methane/air premixed swirling flames enriched with hydrogen has been investigated experimentally with a set of experiments to determine the best way to lower their receptivity to flowrate disturbances without altering significantly the global flow and flame topologies. Both the effects of the hydrogen content and the way this hydrogen is injected in the combustor have been examined either by premixing it with the main mixture or by separate injection of pure hydrogen through a pilot jet at the flame base.

For a fixed thermal power, it has been found that these injection strategies have opposite effects on the flame transfer function and flame describing function. When hydrogen is premixed with the main mixture, the flame shortens and the frequency bandwidth over which the flame is very responsive to incident flow perturbations widens with the hydrogen content in the fuel blend. When hydrogen is injected as a pilot jet at the flame base, it has been shown that the flame is less and less responsive to incident flow perturbations as the hydrogen content increases.

An examination of conditional averages of the flame light emission with respect to the acoustic pulsation revealed that the heat release rate fluctuations produced at the flame base by the pilot hydrogen injection counterbalance in phase opposition the heat release rate fluctuations produced further downstream lowering the global flame response. This mechanism operates at low and high frequencies. For fully premixed methane/hydrogen and air flames, the increased burning velocity of the combustible mixture shortens the flame, but acts the same way on the dynamics at the base and the top of the flame.

This study provides an example on how to lower the flame response to flow perturbations over a broad frequency range and reduce its sensitivity with respect to thermo-acoustic instabilities by adequate injection of small quantities of hydrogen at the base of swirling flames.

The base of a theoretical framework has also been laid to model the acoustic response of flames exhibiting a non-uniform heat release distribution along the reaction layer.

## Acknowledgements

This project has received funding from the European Research Council under the European Union's Horizon 2020 research and innovation programme Grant Agreement 832248, SCIROCCO and under the Horizon 2020, COEC (Center of Excellence in Combustion) program, Grant Agreement 952181.

## References


[1] S. Candel, Combustion dynamics and control: progress and challenges, Proc. Combust. 29 (2002) 1–28.

[2] A. P. Dowling, S. R. Stow, Acoustic analysis of gas turbine combustors, J. Propuls. Power 19 (2003) 751–764.

[3] T. Sattelmayer, W. Polifke, Assessment of methods for the computation of linear stability of combustors, Combust. Sci. Technol. 175 (2003) 453–476.

[4] F. Nicoud, L. Benoit, C. Sensiau, T. Poinsot, Acoustic modes in combustors with complex impedances and multidimensionnal active flames, AIAA J. 45 (2007) 426–441.

[5] S. Camporeale, B. Fortunato, G. Campa, A finite element method for three-dimensional analysis of thermo-acoustic combustion instability, J. Eng. Gas Turb. Power 133 (2011) 011506 (13 pages).

[6] T. Poinsot, Prediction and control of combustion instabilities in real engines, Proc. Combust. Inst. 36 (2017) 1–28.

[7] Preetham, S. Hemchandra, T. Lieuwen, Dynamics of laminar premixed flames forced by harmonic velocity disturbances, J. Prop. Power 24 (2008) 1390–1402.

[8] W. Polifke, Modeling and analysis of premixed flame dynamics by means of distributed time delays, Prog. Energ. Combust. Sci. 79 (2020).

[9] A. Dowling, A kinematic model of a ducted flame, J. Fluid Mech. 394 (1999) 51–72.

[10] N. Noiray, D. Durox, T. Schuller, S. Candel, A unified framework for nonlinear combustion instability analysis based on the flame describing function, J. Fluid Mech. 615 (2008) 139–167.

[11] T. Schuller, T. Poinsot, S. Candel, Dynamics and control of premixed systems based on flame transfer and describing functions, J. Fluid Mech. 894 (2020).

[12] K. Kim, S. Hochgreb, The nonlinear heat release response of stratified lean-premixed flames to acoustic velocity oscillations, Combust. Flame 158 (2011) 2482–2499.

[13] T. Sattelmayer, Influence of the combustor aerodynamics on combustion instabilities from equivalence ratio fluctuations, J. Eng. Gas Turb. Power 125 (2003) 11–19.

[14] T. Komarek, W. Polifke, Impact of swirl fluctuations on the flame response of a perfectly premixed swirl burner, J. Eng. Gas Turb. Power 132 (2010) 061503.

[15] P. Palies, D. Durox, T. Schuller, S. Candel, Experimental study on effects of swirler geometry and swirl number on flame describing functions, Combust. Sci. Technol. 183 (2011) 704–717.

[16] M. Gatti, R. Gaudron, C. Mirat, L. Zimmer, T. Schuller, Impact of swirl and bluff-body on the transfer function of premixed flames, Proc. Combust. Inst. 37 (2019) 5197–5204.

[17] E. Aesoy, H. Nygard, N. Worth, J. Dawson, Tailoring the gain and phase of the flame transfer function through targeted convective-acoustic interference, Combustion and Flame 236 (2022) 111813.

[18] D. Durox, T. Schuller, N. Noiray, S. Candel, Experimental analysis of nonlinear flame transfer functions for different flame geometries, Proc. Combust. Inst. 32 (2009) 1391–1398.

[19] T. Steinbacher, A. Albayrak, A. Ghani, W. Polifke, Consequences of flame geometry for the acoustic response of premixed flames, Combust. Flame 199 (2019) 411–428.

[20] L. Tay-Wo-Chong, W. Polifke, Large eddy simulation-based study of the influence of thermal boundary condition and combustor confinement on premix flame transfer functions, J. Eng. Gas Turb. Power 135 (2013) 021502 (9 pages).

[21] D. Mejia, L. Selle, R. Bazile, T. Poinsot, Wall-temperature effects on flame response to acoustic oscillations, Proc. Combust. Inst. 35 (2015) 3201–3208.

[22] A. Chatelier, T. Guiberti, R. Mercier, N. Bertier, B. Fiorina, T. Schuller, Experimental and numerical investigation of the response of a swirled flame to flow modulations in a non-adiabatic combustor, Flow Turb. Combust. 102 (2019) 995–1023.

[23] S. Barbosa, M. de La Cruz Garcia, S. Ducruix, B. Labegorre, F. Lacas, Control of combustion instabilities by local injection of hydrogen, Proc. Combust. Inst. 31 (2007) 3207–3214.

[24] D. Davis, P. Therkelsen, D. Littlejohn, R. Cheng, Effects of hydrogen on the thermo-acoustics coupling mechanisms of low-swirl injector flames in a model gas turbine combustor, Proc. Combust. Inst. 34 (2013) 3135–3143.

[25] J. Zhang, A. Ratner, Experimental study on the excitation of thermoacoustic instability of hydrogen-methane/ air premixed flames under atmospheric and elevated pressure conditions, Int. J. Hydrogen Energ. 44 (2019) 21324–21335.

[26] T. Indlekofer, A. Byeonguk, Y. Kwah, S. Wiseman, M. Mazur, J. Dawson, N. WOrth, The effect of hydrogen addition on the amplitude and harmonic response of azimuthal instabilities in a pressurized annular combustor, Combustion and Flame 228 (2021) 375–387.

[27] T. Lee, K. Kim, Combustion dynamics of lean fully-premixed hydrogen-air flames in a mesoscale multinozzle array, Combust. Flame 218 (2020) 234–246.

[28] K. Kim, J. Lee, H. Lee, B. Quay, D. Santavicca, Characterization of forced flame response of swirl-stabilized turbulent lean-premixed flames in a gas turbine combustor, J. Eng. Gas Turb. Power 132 (2010).

[29] D. Kim, J. G. Lee, B. D. Quay, D. Santavicca, K. Kim, S. Srinivasan, Effect of flame structure on the flame transfer function in a premixed gas turbine combustor, J. Eng. Gas Turb. Power 132 (2010).

[30] E. Aesoy, J. Aguilar, S. Wiseman, M. Bothien, N. Worth, J. R. Dawson, Scaling and prediction of transfer functions in lean premixed H2 /CH4-flames, Combust. Flame 215 (2020) 269–282.

[31] I. Yilmaz, A. Ratner, M. Ilbas, Y. Huang, Experimental investigation of thermoacoustic coupling using blended hydrogen–methane fuels in a low swirl burner, Int. J. Hydrogen Energ. 35 (2010) 329–336.

[32] T. Hussain, M. Talibi, R. Balachandran, Investigating the effect of local addition of hydrogen to acoustically excited ethylene and methane flames, Int. J. Hydrogen Energ. 44 (2019) 1168–11184.

[33] G. Oztarlik, L. Selle, T. Poinsot, T. Schuller, Suppression of instabilities of swirled premixed flames with minimal secondary hydrogen injection, Combust. Flame 214 (2020) 266–276.

[34] R. Gaudron, M. Gatti, C. Mirat, T. Schuller, Flame Describing Functions of a Confined Premixed Swirled Combustor With Upstream and Downstream Forcing, J. Eng. Gas Turb. Power 141 (2019) 51016–51019.

[35] N. Otsu, A threshold selection method from gray-level histograms, IEEE Trans. Syst. Man Cybern. 9 (1979) 62–66.

[36] R. B. Price, I. R. Hurle, T. M. Sudgen, Optical studies of generation of noise in turbulent flames, Symp. (Int.) Combust. 12 (1968) 1093–1102.

[37] L. Boyer, J. Quinard, On the dynamics of anchored flames, Combust. Flame 82 (1990) 51–65.

[38] P. Palies, D. Durox, T. Schuller, S. Candel, Acoustic-convective mode conversion in an airfoil cascade, J. Fluid Mech. 672 (2011) 545–569.

[39] A. Albayrak, M. P. Juniper, W. Polifke, Propagation speed of inertial waves in cylindrical swirling flows, J. Fluid Mech. 879 (2019) 85–120.

[40] V. Acharya, T. Lieuwen, Effects of azimuthal flow fluctuations on flow and flame dynamics of axisymmetric swirling flames, Phys. Fluids 27 (2015).

[41] A. Albayrak, D. Bezgin, W. Polifke, Response of a swirl flame

to inertial waves, Int. J. Spray Combust. Dyn. 10 (2018) 277–286.
[42] P. Palies, D. Durox, T. Schuller, S. Candel, The combined dynamics of swirler and turbulent premixed swirling flames, Combust. Flame 157 (2010) 1698–1717.
[43] N. A. Bunce, B. D. Quay, D. A. Santavicca, Interaction between swirl number fluctuations and vortex shedding in a single-nozzle turbulent swirling fully-premixed combustor, J. Eng. Gas Turb. Power 136 (2014) 021503.
[44] F. Dupuy, M. Gatti, C. Mirat, Y. Gicquel, F. Nicoud, T. Schuller, Combining analytical models and les data to determine the transfer function from swirled premixed flames, Combust. Flame 217 (2020) 222–236.
[45] D. Laera, P. Agostinelli, L. Selle, Q. Cazères, G. Oztarlik, T. Schuller, L. Gicquel, T. Poinsot, Stabilization mechanisms of ch4 premixed swirled flame enriched with a non-premixed hydrogen injection, Proc. Combust. Inst. 38 (2021) 6355–6363.
[46] M. Gatti, R. Gaudron, C. Mirat, L. Zimmer, T. Schuller, A comparison of the transfer functions and flow fields of flames with increasing swirl levels, in: GT2018-76105, Proceedings of ASME Turbo Expo 2018: Turbomachinery Technical Conference & Exposition.
[47] A. Steinberg, I. Boxx, M. Stöhr, C. Carter, W. Meier, Flow-flame interactions causing acoustically coupled heat release fluctuations in a thermo-acoustically unstable gas turbine model combustor, Combust. Flame 157 (2010) 2250–2266.
[48] F. Luckoff, T. Kaiser, C. Paschereit, K. Oberleithner, Mean field coupling mechanisms explaining the impact of the precessing vortex core on the flame transfer function, Combust. Flame 223 (2021) 254–266.
[49] J. Moeck, J. Bourgouin, D. Durox, T. Schuller, S. Candel, Nonlinear interaction between a precessing vortex core and acoustic oscillations in a turbulent swirl flame, Combust. Flame 159 (2012) 2650–2668.
[50] T. Schuller, D. Durox, S. Candel, A unified model for the prediction of laminar flame transfer functions : comparisons between conical and v-flame dynamics, Combust. Flame 134 (2003) 21–34.
[51] H. Wang, C. Law, T. Lieuwen, Linear response of stretch-affected premixed flames to flow oscillations, Combust. Flame 156 (2009) 889–895.
[52] B. Higgins, M. McQuay, F. Lacas, S. Candel, An experimental study on the effect of pressure and strain rate on ch chemiluminescence of premixed fuel-lean methane/air flames, Fuel 80 (2001) 1583–1591.
[53] B. Higgins, M. McQuay, F. Lacas, J. Rolon, N. Darabiha, S. Candel, Systematic measurements of oh chemiluminescence for fuel-lean, high-pressure, premixed, laminar flames, Fuel 80 (2001) 67–74.
[54] B. Schuermans, F. Guethe, W. Mohr, Optical transfer function measurements for technically premixed flames, J. Eng. Gas Turb. Power 132 (2010).

## Appendix A : Heat release rate fluctuations

The gain and phase lag of PH10 and MH10 responses, with the highest hydrogen content, are presented in Fig. 17 for a modulation level $\tilde{u}_0/\overline{u}_0 = 0.10$. Results obtained for $CH^*$ and $OH^*$ light intensity are identical independently of the strategy used to inject hydrogen. The same experiments were repeated for the other cases and for other forcing levels. Results based on $CH^*$ and $OH^*$ signals were again found to be identical confirming that both can be used to analyze the flame response. This is why only results with $CH^*$ are presented in this study.

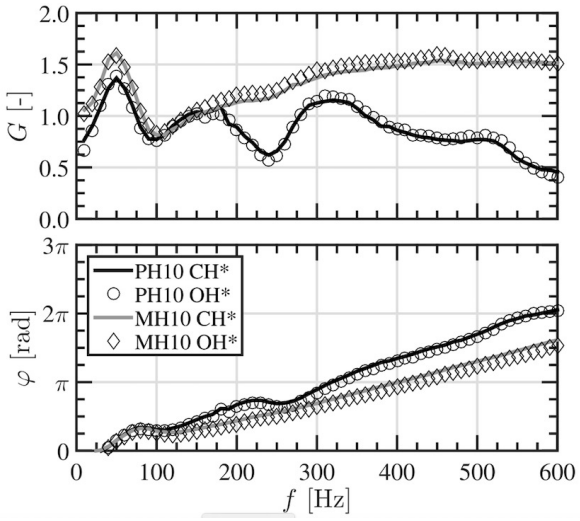


Figure 17: Comparison of the MH10 and PH10 flame responses measured with $CH^*$ or $OH^*$ emissions. Pulsation level $\tilde{u}_0/\overline{u}_0 = 0.1$.

Comparing the premixed MH10 and pilot PH10 cases in Fig. 17, their gain and phase responses rapidly differ as the forcing frequency increases. For the premixed MH10 case, relative fluctuations of light intensity also correspond to relative fluctuations of the heat release rate.

Two series of experiments are conducted with a $CH^*$ filter in which the photomultiplier gain is adjusted to always yield the same signal $I_{CH^*} = 3.9$ V for $\dot{Q} = 3.9$ kW at $\phi = 0.8$ and all the tested injection strategies. In the first series of experiments, the equivalence ratio is kept constant at $\phi = 0.8$ and the heat release rate $\dot{Q}$ is varied by assuming complete combustion with:

$$\phi = s\frac{\dot{m}_{CH_4} + \dot{m}_{H_2}}{\dot{m}_a} \quad (11)$$

$$\dot{Q} = \dot{m}_{CH_4}\Delta h_{CH_4} + \dot{m}_{H_2}\Delta h_{H_2} \quad (12)$$

where $\dot{m}_f$ and $\Delta h_f$ with $f = CH_4$ or $H_2$ designate the fuel mass flowrate and its heat value respectively, $\dot{m}_a$ the air mass flowrate and $s$ corresponds the ratio $\dot{m}_a/(\dot{m}_{CH_4}+\dot{m}_{H_2})$ at stoichiometry. For the pilot injection cases, $\phi$ designates the equivalence ratio of the combustible mixture if hydrogen would have been perfectly mixed with methane and air.

Figure 18(a) shows that the $CH^*$ intensity $I$ linearly increases with $\dot{Q}$ for all cases. Measurements for the hydrogen enriched mixture MH10 fall on the same line

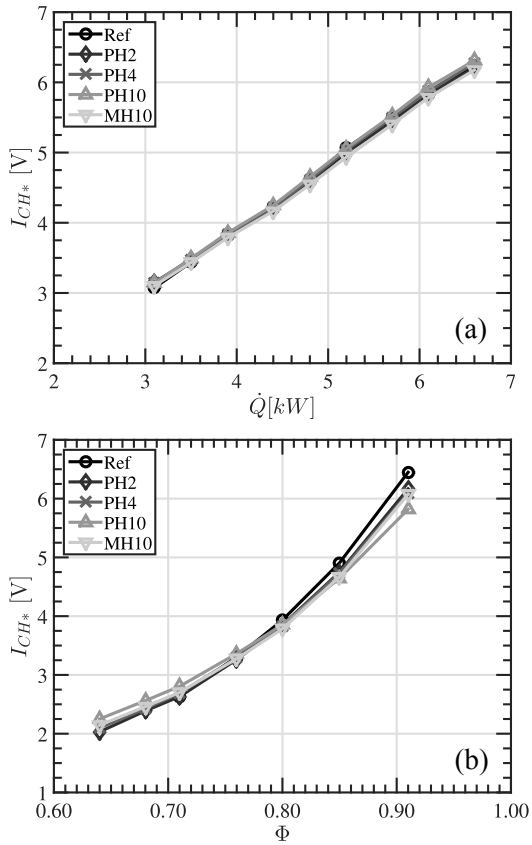


Figure 18: CH* intensity as a function of (a) flame power $\dot{Q}$ for a fixed equivalence ratio $\phi = 0.8$ and (b) equivalence ratio $\phi$ for a fixed flame power $\dot{Q} = 3.9$ kW.

as the Ref case. The same is observed for the MH4 mixture, not shown here, indicating that mixing hydrogen within the methane/air mixture does not modify the slope of the response when the mixture composition remains fixed. The same observations are made for the PH2, PH4 and PH10 cases in Fig. 18(a) when the central hydrogen jet is not perfectly mixed with the annular methane/air mixture at the burner outlet. Despite the redistribution of the flame luminosity towards the flame root with pilot hydrogen injection, Fig. 18(a) confirms that the global flame luminosity follows the same scaling law for all tested cases. This property ceases however for higher hydrogen mass flowrates injected through the pilot tube with a progressive departure from the Ref case.

The second series of experiments is carried out at constant flame power $\dot{Q}$ by varying the global equivalence ratio $\phi$. Results in Fig. 18(b) deviate from a single curve when the hydrogen concentration is increased or when the hydrogen injection strategy is modified.

In the same line of reasoning as in [52–54], Figs. 18(a) and (b) suggest the following link between the CH* intensity and the heat release rate:

$$I = k\dot{Q}\phi^{\beta} \tag{13}$$

The values of the parameters $k$ and $\beta$ depend on the case explored and are reported in Tab. 2. Experiments were repeated by recording the OH* chemiluminescence intensity that was found to obey to the same governing law, but with slightly different values for the $k$ and $\beta$, which are not reported here.

Equation (13) is now used to analyze the origin of heat release rate disturbances by assuming it remains valid when the annular flow is submitted to acoustic disturbances around the nominal operating condition $\overline{\dot{Q}} = 3.9$ kW and $\phi = 0.8$. Heat release rate disturbances $\widetilde{\dot{Q}}$ may then be deduced from CH* intensity fluctuations $\tilde{I}$ using the following quasi-steady approximation for small perturbations:

$$\frac{\widetilde{\dot{Q}}}{\overline{\dot{Q}}} = \frac{\tilde{I}}{\overline{I}} - \beta\frac{\tilde{\phi}}{\overline{\phi}} \tag{14}$$

In this expression, $\widetilde{\dot{Q}}$ and $\tilde{I}$ denote the Fourier components of the signals at forcing frequency $f$ and $\overline{\dot{Q}}$ and $\overline{I}$ their mean values. For fully premixed operating conditions in which the mixture composition remains constant, i.e. $\tilde{\phi} = 0$, flames are only submitted to flowrate disturbances. One retrieves in this case the classical relationship $\dot{Q}/\overline{\dot{Q}} = \tilde{I}/\overline{I}$ valid for the methane/air Ref case and the premixed hydrogen enriched MH4 and MH10 flames.

In configurations with pilot fuel injection, the methane/air mixture in the annular channel is submitted to flowrate disturbances due to the acoustic forcing, but the hydrogen mass flowrate in the central tube remains fixed. As a consequence, these flames are submitted to both flow rate and mixture composition oscillations at the burner outlet and the resulting heat release rate disturbances $\tilde{\dot{Q}}$ are no longer proportional to the CH*, or OH*, light intensity $\tilde{I}$.

By recognizing that for the perturbed PH2, PH4 and PH10 cases, there are no disturbances of the hydrogen mass flowrate, $\widetilde{\dot{m}}_{H_2} = 0$, equivalence ratio fluctuations at the burner outlet are only due to fluctuations of the methane and air mass flow rates inside the annular channel:

$$\frac{\tilde{\phi}}{\overline{\phi}} = \frac{\widetilde{\dot{m}}_{CH_4}}{\overline{\dot{m}}_{CH_4} + \overline{\dot{m}}_{H_2}} - \frac{\widetilde{\dot{m}}_a}{\overline{\dot{m}}_a} = (Y_{CH_4} - 1)\frac{\widetilde{\dot{m}}_a}{\overline{\dot{m}}_a} \tag{15}$$

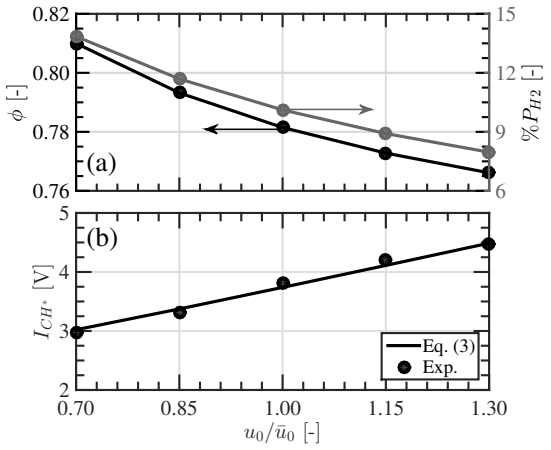


Figure 19: (a) Change of the equivalence ratio $\phi$ and fraction of power originating from hydrogen combustion $P_{H_2}$ as function of the bulk velocity $u_0$ in the annular channel around the PH10 operating condition corresponding to $P = 3.9$ kW, $\phi = 0.78$ and $P_{H_2} = 10\%$. (b) Predictions from Eq. (13) are compared to measurements.

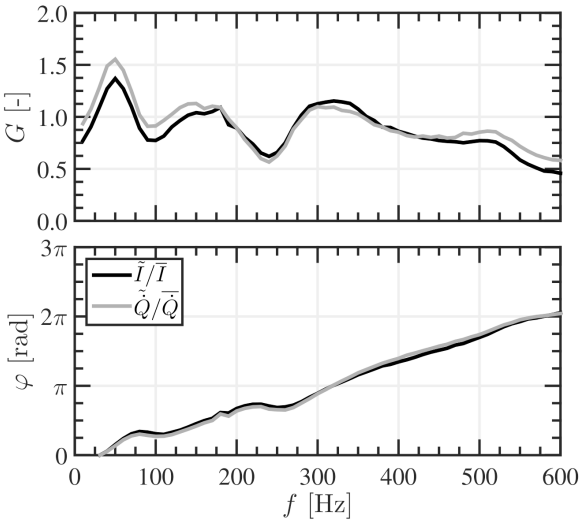


Figure 20: PH10 flame response determined with the CH* light intensity and the heat release rate $\dot{Q}$. Pulsation level $\tilde{u}_0/\bar{u}_0 = 0.1$.

where $Y_{CH_4}$ denotes the methane mass fraction in the methane/hydrogen fuel blend. The last equality in Eq. (15) holds because the equivalence ratio of the methane air mixture in the annular channel remains fixed. In these conditions, heat release rate fluctuations from the disturbed pilot hydrogen enriched flames may be deduced from light intensity fluctuations $\tilde{I}$ and acoustic velocity modulations $\tilde{u}$ at the burner outlet with Eq. (1) that is reproduced here:

$$\frac{\widetilde{\dot{Q}}}{\bar{\dot{Q}}} = \frac{\tilde{I}}{\bar{I}} + \beta Y_{H2} \frac{\tilde{u}_0}{\bar{u}_0} \tag{16}$$

In this latter expression, it has been assumed that density disturbances could be neglected compared to acoustic velocity fluctuations $\tilde{u}_0$ at the burner outlet in the low Mach number flow using $\widetilde{\dot{m}_a}/\bar{\dot{m}}_a = \tilde{u}_0/\bar{u}_0$.

A last test is reported to show that Eq. (16) remains valid when both the equivalence ratio and the fraction of hydrogen are varied. The model Eq. (13) for the chemiluminescence intensity $I_{CH^*}$ assumes that the impact of the hydrogen injection strategy only modifies the signal $I_{CH^*}$ through changes of the lump coefficients $k$ and $\beta$ as described in Tab. 2. Experiments used to determine these coefficients were carried out at fixed fractions of power $P_{H_2}$ originating from hydrogen combustion. More specifically, when the equivalence ratio $\phi$ was varied, the fraction of power originating from hydrogen combustion $P_{H_2}$ was held constant.

However, during acoustic forcing of flames with hydrogen pilot injection, the hydrogen flow rate remains fixed in the central injection channel and modulations of the methane/air flow rate in the annular channel lead consequently to fluctuations of the equivalence ratio $\phi$ in which the hydrogen content varies.

Figure 19(a) shows how the equivalence ratio $\phi$ and the hydrogen power content $P_{H_2}$ are altered with respect to the unperturbed configuration when the bulk velocity $u_0$ in the annular channel is modified by ±30% as when the flame is submitted to acoustic excitation during a forcing cycle with a modulation level $\tilde{u}_0/\bar{u}_0 = 0.3$. The selected unperturbed configuration corresponds here to PH10, i.e. $P = 3.9$ kW, $\phi = 0.78$ and $P_{H_2} = 10\%$.

Figure 19(b) plots measurements of the chemiluminescence intensity $I_{CH^*}$ corresponding to the operating conditions shown in Fig. 19(a). Predictions from Eq. (13) are also plotted with the lump parameter values set to $k = 1.91$ and $\beta = 2.82$ corresponding to the PH10 configuration in Tab. 2. Predictions match well measurements. This additional test shows that Eq. (13) is appropriate to analyze the response of the flames with pilot hydrogen injection that are explored in this study.

Figure 20 shows the PH10 flame response determined with the CH* intensity $\tilde{I}/\bar{I}$ in gray, which is compared to the flame response determined with the reconstructed heat release rate signal deduced from Eq. (16). One can see that the correction only slightly modifies the FTF gain and barely changes the phase lag.

## Appendix B : Derivation of the FTF model

The FTF model appearing in Eq. (10) is derived in this section. It relies on a kinematic description for

flame wrinkles that propagate along the inclined reaction layer shown in Fig. 15 when it is submitted to velocity disturbances in the fresh stream of reactants [7, 8, 11, 37].

In order to simplify the derivation, one here considers a uniform axial flow of velocity $\bar{u}_0$ in an annular channel of internal radius $a$ and external radius $b$ as sketched in Fig. 15. The flame sheet makes an angle $\alpha$ with respect to the axial flow direction $z$ and one assumes a given distribution of the heat release rate per unit flame area $\overline{\dot{q}}$ along this flame sheet that only depends on the distance $z$ to the injector outlet. For the perturbed flow field, one retains the simplest disturbed velocity field by assuming that the flame is submitted to a uniform velocity modulation $\tilde{u} = \tilde{u}_0$.

With these hypotheses, the perturbed normal displacement $\tilde{\xi}$ with respect to the mean flame position is given by [50]:

$$\frac{\tilde{\xi}\cos\alpha}{b-a} = \frac{\tilde{u}_0}{\overline{u}_0}\left[\exp\left(i\omega_*\frac{y}{H}\right)-1\right] \tag{17}$$

where $\omega_* = \frac{\omega H}{\overline{u}_0}\frac{1}{\cos^2\alpha}$ is a dimensionless frequency.

One may then deduce the FTF of a fully premixed V-shaped flame featuring a uniform heat release rate distribution $\overline{\dot{q}} = \dot{q}_0$ along the reaction layer by integration of Eq. (17) [9, 50]:

$$\frac{\widetilde{\dot{Q}}}{\overline{\dot{Q}}} = \frac{\int\overline{\dot{q}}d\tilde{A}}{\int\overline{\dot{q}}d\overline{A}} = \frac{\tilde{A}}{\overline{A}} = FTF_{\gamma=0}\frac{\tilde{u}_0}{\overline{u}_0} \tag{18}$$

where

$$\begin{aligned} FTF_{\gamma=0} &= 2\frac{b-a}{b+a}\Big[\frac{b}{b-a}\frac{1}{i\omega_*}\left(\exp(i\omega_*)-1\right) \\ &+ \frac{1}{\omega_*^2}\left(\exp(i\omega_*)-1-i\omega_*\right)\Big] \end{aligned} \tag{19}$$

This procedure is now extended to the case of a flame sheet with a non uniform heat release distribution that linearly varies along the flame branch:

$$\overline{\dot{q}} = \frac{\dot{q}_0}{c}\left(1+\gamma\frac{z}{H}\right) \tag{20}$$

In this expression $\gamma$ and $c$ are constant parameters. The value for $c$ is chosen in order to investigate flames featuring the same mean global heat release rate $\overline{\dot{Q}}$ and the same mean flame surface area $\overline{A}$:

$$\overline{\dot{Q}} = \int\overline{\dot{q}}d\overline{A} = \overline{A}\frac{\dot{q}_0}{c}\left[1+\gamma\left(\frac{a}{b+a}+\frac{2}{3}\frac{b-a}{b+a}\right)\right] \tag{21}$$

where $\overline{A} = \pi(b^2-a^2)/\sin\alpha$. In order to satisfy $\overline{\dot{Q}} = \dot{q}_0\overline{A}$, the coefficient $c$ needs to be fixed to $c = 1+\gamma\left(\frac{a}{b+a}+\frac{2}{3}\frac{b-a}{b+a}\right)$.

The heat release rate disturbance is obtained by integration of flame wrinkles along the mean reaction layer:

$$\widetilde{\dot{Q}} \simeq \int\overline{\dot{q}}d\tilde{A} \tag{22}$$

In this expression, the second term $\int\tilde{\dot{q}}d\overline{A}$ has been discarded by assuming that perturbations of the burning intensity $\tilde{\dot{q}}$ remain small compared to flame surface area fluctuations. For premixed flames kept at constant equivalence ratio, this hypothesis is reasonable because the fuel burning flux $f = \dot{q}/(-\Delta h_f^0)$, where $-\Delta h_f^0$ is the fuel heat value per unit mass, remains essentially constant. For partially premixed systems or more generally systems where the mixture composition may fluctuate, this approximation does not hold because fluctuations of $f$ and $dA$ are of the same order of magnitude. In the cases considered in this study, it has been shown that perturbations of the mixture composition remain small and Eq. (22) is assumed to be valid.

An infinitesimal fluctuation of the flame surface area is linked to the perturbed flame displacement appearing in Eq. (17) by $d\tilde{A} = 2\pi(z+a/\tan\alpha)d\tilde{\xi}$ leading to:

$$\int\overline{\dot{q}}d\tilde{A} = 2\pi\int_0^H\overline{\dot{q}}zd\tilde{\xi} + 2\pi\frac{a}{b-a}H\int_0^H\overline{\dot{q}}d\tilde{\xi} \tag{23}$$

Combining the previous expressions, one may write:

$$\frac{\widetilde{\dot{Q}}}{\overline{\dot{Q}}} = \frac{1}{c}\left[FTF_{\gamma=0}+\gamma FTF_{\gamma\neq0}\right]\frac{\tilde{u}_0}{\overline{u}_0} \tag{24}$$

where:

$$\begin{aligned} FTF_{\gamma\neq0} &= \left(\frac{\tilde{A}_{\gamma\neq0}}{\overline{A}}\right)\Big/\left(\frac{\tilde{u}_0}{\overline{u}_0}\right) \\ &= \frac{2\pi}{H}\int_0^H z^2d\tilde{\xi} + 2\pi\frac{a}{b-a}\int_0^H zd\tilde{\xi} \end{aligned} \tag{25}$$

After integration, one finally obtains:

$$\begin{aligned} FTF_{\gamma\neq0} = \frac{2}{i\omega_*}\Big[\frac{b-a}{b+a}\Big(\exp(i\omega_*)-2\Big(\frac{\exp(i\omega_*)}{i\omega_*} \\ +\frac{\exp(i\omega_*)-1}{\omega_*^2}\Big)\Big)+\frac{a}{b+a}\left(\exp(i\omega_*)-\frac{\exp(i\omega_*)-1}{i\omega_*}\right)\Big] \end{aligned} \tag{26}$$